

Article

A Molten-Salt Pyrolysis Synthesis Strategy toward Sulfur-Functionalized Carbon for Elemental Mercury Removal from Coal-Combustion Flue Gas

Jianping Yang¹, Hong Xu¹, Fanyue Meng¹ , Qingjie Guo², Tao He³, Zequn Yang¹, Wenqi Qu¹ and Hailong Li^{1,*}

- ¹ School of Energy Science and Engineering, Central South University, Changsha 410083, China; jpyang@csu.edu.cn (J.Y.); xh18@foxmail.com (H.X.); mfy19941029@163.com (F.M.); zequn_yang@hotmail.com (Z.Y.); wenqiqu1984@163.com (W.Q.)
- ² State Key Laboratory of High-Efficiency Utilization of Coal and Green Chemical Engineering, Ningxia University, Yinchuan 750021, China; qingjie_guo@nxu.edu.cn
- ³ Shandong Shiheng Thermal Power Co., Ltd., Taian 271600, China; hthetao1988@163.com
- * Correspondence: hailongli18@gmail.com; Tel.: +86-18670016725; Fax: +86-731-88879863

Abstract: The emission of mercury from coal combustion has caused consequential hazards to the ecosystem. The key challenge to abating the mercury emission is to explore highly efficient adsorbents. Herein, sulfur-functionalized carbon (S-C) was synthesized by using a molten-salt pyrolysis strategy and employed for the removal of elemental mercury from coal-combustion flue gas. An ideal pore structure, which was favorable for the internal diffusion of the Hg⁰ molecule in carbon, was obtained by using a SiO₂ hard template and adjusting the HF etching time. The as-prepared S-C with an HF etching time of 10 h possessed a saturation Hg⁰ adsorption capacity of 89.90 mg·g⁻¹, far exceeding that of the commercial sulfur-loaded activated carbons (S/C). The S-C can be applied at a wide temperature range of 25–125 °C, far exceeding that of commercial S/C. The influence of flue gas components, such as SO₂, NO, and H₂O, on the Hg⁰ adsorption performance of S-C was insignificant, indicating a good applicability in real-world applications. The mechanism of the Hg⁰ removal by S-C was proposed, i.e., the reduced components, including sulfur thiophene, sulfoxide, and C-S, displayed a high affinity toward Hg⁰, which could guarantee the stable immobilization of Hg⁰ as HgS in the adsorbent. Thus, the molten-salt pyrolysis strategy has a broad prospect in the application of one-pot carbonization and functionalization sulfur-containing organic precursors as efficient adsorbents for Hg⁰.

Keywords: mercury; adsorption; carbon; molten salt; coal combustion



Citation: Yang, J.; Xu, H.; Meng, F.; Guo, Q.; He, T.; Yang, Z.; Qu, W.; Li, H. A Molten-Salt Pyrolysis Synthesis Strategy toward Sulfur-Functionalized Carbon for Elemental Mercury Removal from Coal-Combustion Flue Gas. *Energies* **2022**, *15*, 1840. <https://doi.org/10.3390/en15051840>

Academic Editors: Roberto Alonso González Lezcano, Francesco Nocera and Rosa Giuseppina Caponetto

Received: 29 January 2022

Accepted: 27 February 2022

Published: 2 March 2022

Publisher's Note: MDPI stays neutral with regard to jurisdictional claims in published maps and institutional affiliations.



Copyright: © 2022 by the authors. Licensee MDPI, Basel, Switzerland. This article is an open access article distributed under the terms and conditions of the Creative Commons Attribution (CC BY) license (<https://creativecommons.org/licenses/by/4.0/>).

1. Introduction

The excessive emission of mercury from industrial activities has caused consequential hazards to the ecosystem and human health [1–3]. Coal combustion is one of the largest industrial sources of mercury emission. The mercury emitted from typical coal-combustion flue gas generally existed in three forms, i.e., elemental mercury (Hg⁰), oxidized mercury (Hg²⁺), and particulate bound mercury (Hg^p) [4–8]. The Hg^p can be captured by using particulate matter control devices, while the Hg²⁺ can be removed by using wet flue-gas scrubbers due to Hg²⁺'s water solubility [9–12]. However, Hg⁰ is difficult to remove owing to its water insolubility and high volatility [13–15]. As a consequence, Hg⁰ is the primary species of mercury discharged into the atmosphere from coal-combustion flue gases. The highly efficient removal of Hg⁰ is a key challenge to reducing mercury pollution from coal-fired power plants.

Activated carbons (ACs) are the most widely researched and skilled mercury adsorbents for coal-fired power plants [16–21]. However, ACs were generally limited by

adsorption kinetics and equilibrium capacities, hence causing large consumptions of ACs during Hg^0 removal [22,23]. Moreover, the weak binding affinity of ACs toward mercury induced leaching risks of mercury when the ACs were dumped in landfills together with fly ashes [24,25]. Thus, active components that can accommodate Hg^0 were generally introduced to the ACs to improve the Hg^0 adsorption capacity. In nature, the mercury was tied to sulfides owing to its sulphophile affinity [26,27]. Inspired by this natural law, sulfur was widely employed to modify the Hg^0 adsorption capacity of ACs [28,29]. This strategy was relatively simple, cheap, and effective, but was still found to suffer from drawbacks [30,31]. The most significant one is that the sulfur was not actually anchored to the carbon surface during the impregnation process, hence affecting the activity, abundance, and accessibility of the sulfur groups during Hg^0 removals [32]. The impregnation method for introducing sulfur would plug the pores of ACs. As a result, the efficient diffusion of Hg^0 on the sulfur-modified ACs would be limited [33]. In addition, the anchoring of sulfur on ACs was not firm, hence causing leaching risks of sulfur as well as mercury adsorption products when ACs were disposed of in landfills [32,34]. Therefore, a new strategy is urgently undergoing exploration to overcome the disadvantages associated with sulfur-impregnated ACs [35,36].

Traditionally, the sulfur-functionalized carbon materials were prepared by using two steps, i.e., the carbonization of natural products (e.g., cellulose, chitin, starch, alginate, and chitosan) as well as some synthetic polymers (e.g., poly-acrylonitrile, polyaniline, and phenolic resins) first and then introducing sulfur onto carbons by using an impregnation method [37–40]. A one-pot carbonization and functionalization step, which could guarantee the uniform distribution and firm fixation of sulfur functionality on the carbon matrix, was required. Very recently, a simple approach via the carbonization of small organic molecules with the assistance of transition metals was reported to prepare a series of functional carbon materials [37]. This approach was realized via the pyrolysis of a mixture of small organic molecules and transition-metal salts in a conventional tubular furnace, hence avoiding the barriers to large-scale production, such as complicated equipment and harsh conditions. The salts would act as a heat-transfer medium and provide an oxygen-free environment for pyrolysis [41]. Moreover, the salts catalyze the formation of a thermally stable intermediate polymerization structure, avoiding the direct sublimation of small organic molecules during heating [37,38]. More attractive, template-like SiO_2 could be mixed into the precursors and hence adopted to adjust the porosity of carbons. This strategy is commonly available and easy to use to control the surface sulfur functionalities, porosities, and morphologies of carbons.

In this work, porous sulfur-functionalized carbons were prepared and employed for Hg^0 removal from coal-fired flue gas. The removal performance of sulfur-functionalized carbon (S-C) on Hg^0 was studied and compared with that of commercial sulfur-loaded ACs (S/C). The Hg^0 removal performances of S-C and S/C under various adsorption temperatures and flue gas conditions were studied. The excellent adsorption mechanism of Hg^0 by S-C was further investigated. This work not only provides a promising trap for highly efficient Hg^0 sequestration from coal-fired power plants but also illustrates a versatile platform for preparing functional carbon materials by using a one-pot carbonization and functionalization organic precursor.

2. Experimental Section

2.1. Sample Preparation

S-C was prepared by using a molten-salt pyrolysis strategy [38]. Two grams of 2,2-bithiophene and 2.0 g of SiO_2 were added into 150 mL of tetrahydrofuran and stirred at room temperature for 6 h. The mixture was then dried and then ground to a powder. After that, the powder was placed into a rail boat and covered with 5.0 g of $\text{Co}(\text{NO}_3)_2 \cdot 6\text{H}_2\text{O}$, which was heated at 800 °C for 2 h. Then, the SiO_2 was removed by using 10% HF solution. To obtain different porosity of S-C, the sample was etched by using HF for different times (0, 24, 48 and 56 h). After drying at 105 °C for 10 h, the S-C was finally obtained.

2.2. Sample Characterization

The morphology of the sample was studied by using a scanning electronic microscope (SEM, FEI F50, New York, NY, USA). Transmission electron microscope (TEM, EOL JEM 2100F, microscope Tokyo, Japan) and high-resolution TEM (HRTEM) were used to study the morphology and structure of sample. The valence states of samples were characterized by using X-ray photoelectron spectroscopy (XPS, Thermo ESCALAB 250Xi, New York, NY, USA).

2.3. Hg⁰ Adsorption Activity Tests

The Hg⁰ adsorption activity test was measured on a fixed-bed reactor [42,43]. The adsorbent was placed in a quartz reactor, reaction temperature of which was controlled by using a tube furnace. The flue gas was composed of N₂, O₂, SO₂, NO, and H₂O, with the total flow rate of 1 L·min⁻¹. Hg⁰ was provided by a mercury permeation tube placed in a constant temperature water bath, delivering Hg⁰ by using N₂ to ensure a stable concentration of 65 µg·m⁻³. The concentration of Hg⁰ was monitored by using an online mercury analyzer (RA-915M, Lumex, Tianjin, China). The Hg⁰ adsorption capability was calculated by using the following equations:

$$Q = \frac{1}{m} \int_{t_1}^{t_2} (C_{in} - C_{out}) \times f \times dt \quad (1)$$

where C_{in} (µg·m⁻³) and C_{out} (µg·m⁻³) represent the inlet and outlet concentrations of Hg⁰, Q (µg·g⁻¹) is the Hg⁰ adsorption capacity, m (g) is the sample amount, f (m³·h⁻¹) is the gas flow rate, and t (h) is the reaction time.

3. Description of Sorption Kinetic Models

3.1. Pseudo-First-Order Model

This model is described as follows [44]:

$$\frac{dq_t}{dt} = k_1(q_e - q_t) \quad (2)$$

Based on the initial conditions, i.e., $t = 0$ $q_t = 0$, Equation (2) is revised as:

$$q_t = q_e(1 - e^{-k_1 t}) \quad (3)$$

where q_t and q_e represent the adsorbed mercury amount at any time t and equilibrium time (µg·g⁻¹). k_1 represents the rate constant (min⁻¹).

3.2. Pseudo-Second-Order Model

This model is described as follows [45]:

$$\frac{dq_t}{dt} = k_2(q_e - q_t)^2 \quad (4)$$

On the basis of initial conditions, i.e., $t = 0$ and $q_t = 0$, Equation (4) is modified as:

$$q_t = \frac{t}{\frac{1}{k_2 q_e^2} + \frac{1}{q_e} t} \quad (5)$$

where k_2 represents the rate constant (µg/(cm³·min)).

3.3. Elovich Model

This model is described as follows [46]:

$$\frac{dq_t}{dt} = \alpha \exp(-\beta q_t) \quad (6)$$

where α represents the initial rate and β is related to surface coverage and activation energy. If t is much larger than t_0 , this equation is modified as follows:

$$q_t = \frac{1}{\beta} \ln(\alpha\beta) + \left(\frac{1}{\beta}\right) \ln t \quad (7)$$

3.4. Intra-Particle Diffusion Model

This model is described by the following formula [47]:

$$q_t = k_{id}t^{0.5} + C \quad (8)$$

where k_{id} represents the diffusion rate constant within the particle and C is a constant, which is related to the boundary layer.

4. Results and Discussion

4.1. Preparation and Characterization of Samples

The S-C was prepared by using the molten $\text{Co}(\text{NO}_3)_2 \cdot 6\text{H}_2\text{O}$ -assisted carbonization of sulfur-containing small organic molecule precursors. SiO_2 nanoparticles were adopted as hard templates, followed by an HF etching step to remove the SiO_2 template. The porosity of S-C was adjusted by using the HF etching time (shown in Figure 1). As listed in Table 1, the HF etching step will generate mesopores on the S-C. The S-C with HF etching for 10 h possessed the largest BET surface area of $318.5 \text{ m}^2 \cdot \text{g}^{-1}$, with an average pore size of 7.31 nm and total pore volume of $0.58 \text{ cm}^3 \cdot \text{g}^{-1}$. Pore size affects the internal mass transfer process of Hg^0 on adsorbents, thus affecting the removal rate of Hg^0 . As shown in Figure 2a, the N_2 absorption–desorption isotherms for S-C belonged to a typical II isotherm, indicating that the porosity of S-C was very limited. The S-C after the HF etching step presented a typical IV isotherm with a negligible absorption at lower pressures but significant absorption at higher pressures ($p/p^0 = 0.2\text{--}1.0$). This indicates that S-C is composed of mesopores or macropores rather than micropores. The pore distribution curves shown in Figure 2b demonstrate that the pore size of the S-C was in the range of 2–10 nm. The mesoporous structure in the range of 2–50 nm is beneficial for Hg^0 's diffusion to the inner surface of an adsorbent [48]. Thus, the pore structure of S-C is favorable for Hg^0 adsorption.

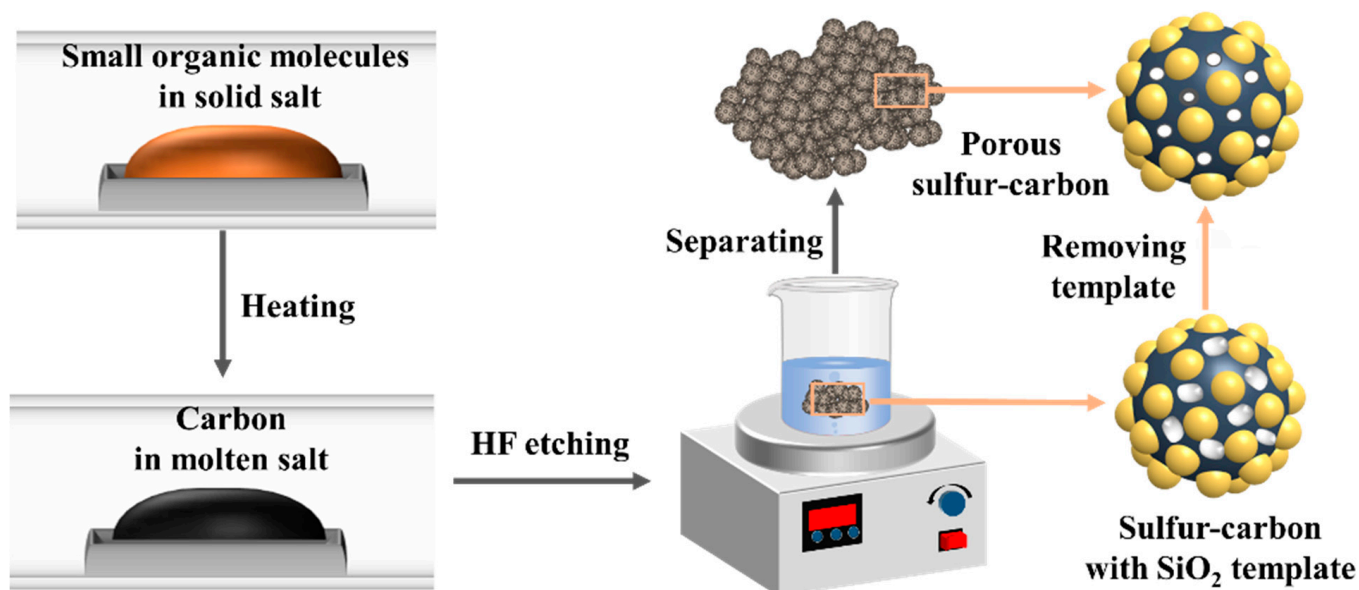


Figure 1. Schematic illustration of the synthesis process for S-C.

Figure 3 shows the morphologies of S-Cs with different HF etching times. These images display the high-resolution local microscopies of individual particles, in which the

sizes of individual particles are in the range of 100–200 mesh. As shown, the morphology of S-C was significant dependent on the HF etching time. The S-C without HF etching displayed a dense surface, and there were negligible pores observed on the S-C surface. After etching with HF, abundant pores were generated on the S-C surface, and more pores were generated with the extension of the HF etching time from 5 to 10 h. Thus, the SiO₂ was embedded in the carbon structure as a template, which could be removed by using the HF solution to induce the formation of a porous structure. However, upon reaching a higher HF etching time, the resultant carbon framework collapsed, which might have affected the internal diffusion of mercury. Therefore, a SiO₂ template was used to achieve the adjustable preparation of porous carbons.

Table 1. Pore structure parameters of various S-Cs with different HF etching times.

HF Etching Time (h)	Total Surface Area (m ² ·g ⁻¹)	Surface Area of Micropores (m ² ·g ⁻¹)	Pore Volume (cm ³ ·g ⁻¹)	Pore Diameter (nm)
0	180.92	143.33	0.29	6.32
5	267.66	263.68	0.50	7.43
10	318.50	335.88	0.58	7.31

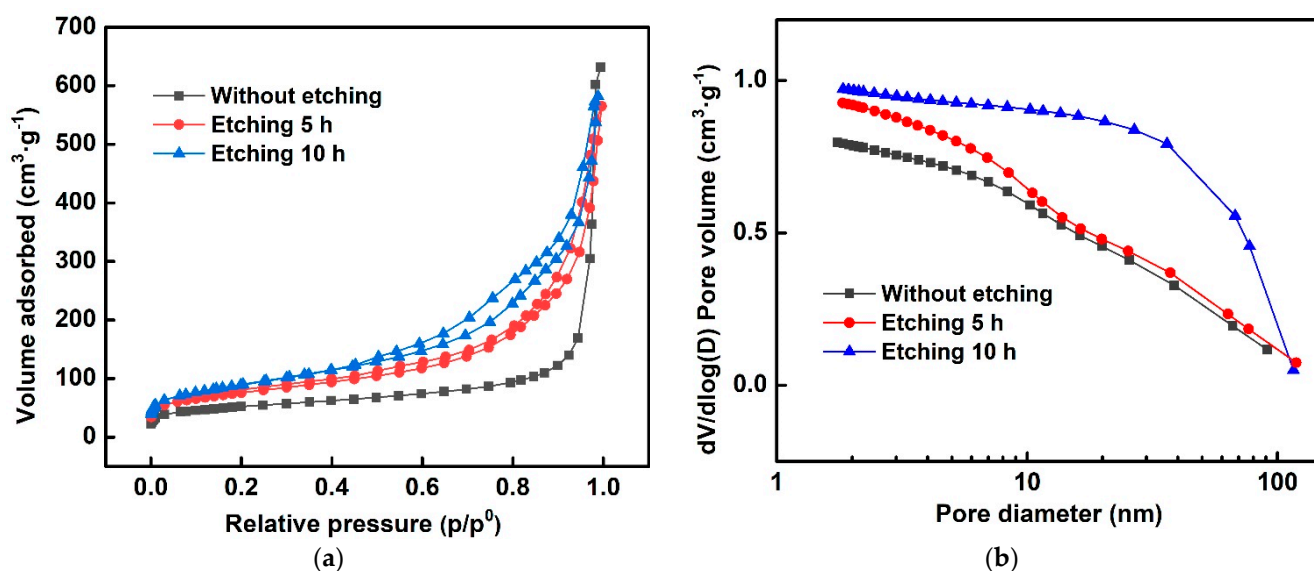


Figure 2. (a) N₂ adsorption–desorption isotherms and (b) pore size distributions of S-C.

The surface-functional groups of S-C were studied by using FTIR. As shown in Figure 4, there were four main peaks on the FTIR spectra, which could be assigned to the C-OH (3392 and 615 cm⁻¹) and aromatic C = C (1626 and 1100 cm⁻¹) [49]. Figure 5 shows the XPS spectra for S-C. As shown in Figure 5a, the spectra for high-resolution C 1s spectra could be divided into three peaks at 284.8, 286.0, and 288.8 eV, assigned to the characteristic peaks of C = C, C-O, and C = O [30]. Figure 5b shows the O 1s spectra for C-S, in which the peaks at 531.5, 532.3, and 533.3 eV are regarded as C-OH, C-O, and O-H [31]. Figure 5c shows the S spectra for S-C. The sulfur on the S-C existed in four forms. The two peaks at 164.2 and 165.3 eV corresponded to S 2p_{3/2} and S 2p_{1/2} for thiophenic sulfur (i.e., -C-S_x-C-, x = 1-2), the small peak at 169.1 eV could be assigned to sulfoxide [50], the peak at 166.2 eV could be assigned to C-S, while the peaks at 167.2 and 170.3 eV could be assigned to sulfate [51,52].

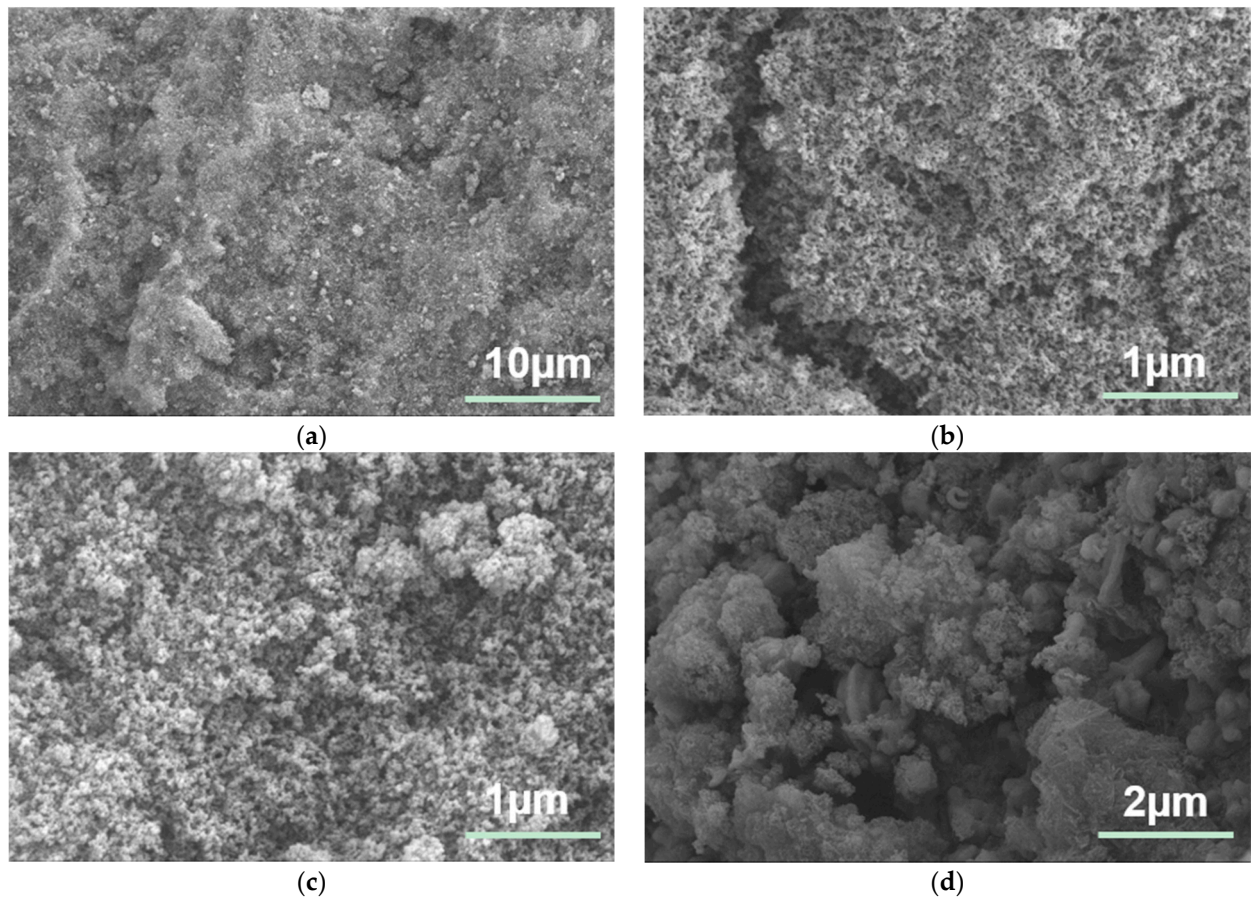


Figure 3. SEM images of S-C with HF etchings for (a) 0 h, (b) 5 h, (c) 10 h, and (d) 20 h.

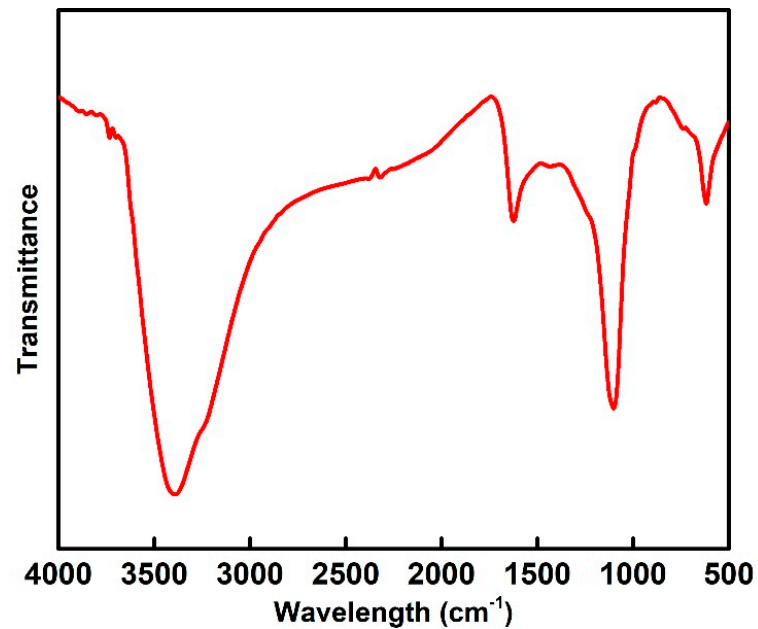


Figure 4. FTIR spectra of the synthetic S-C sample.

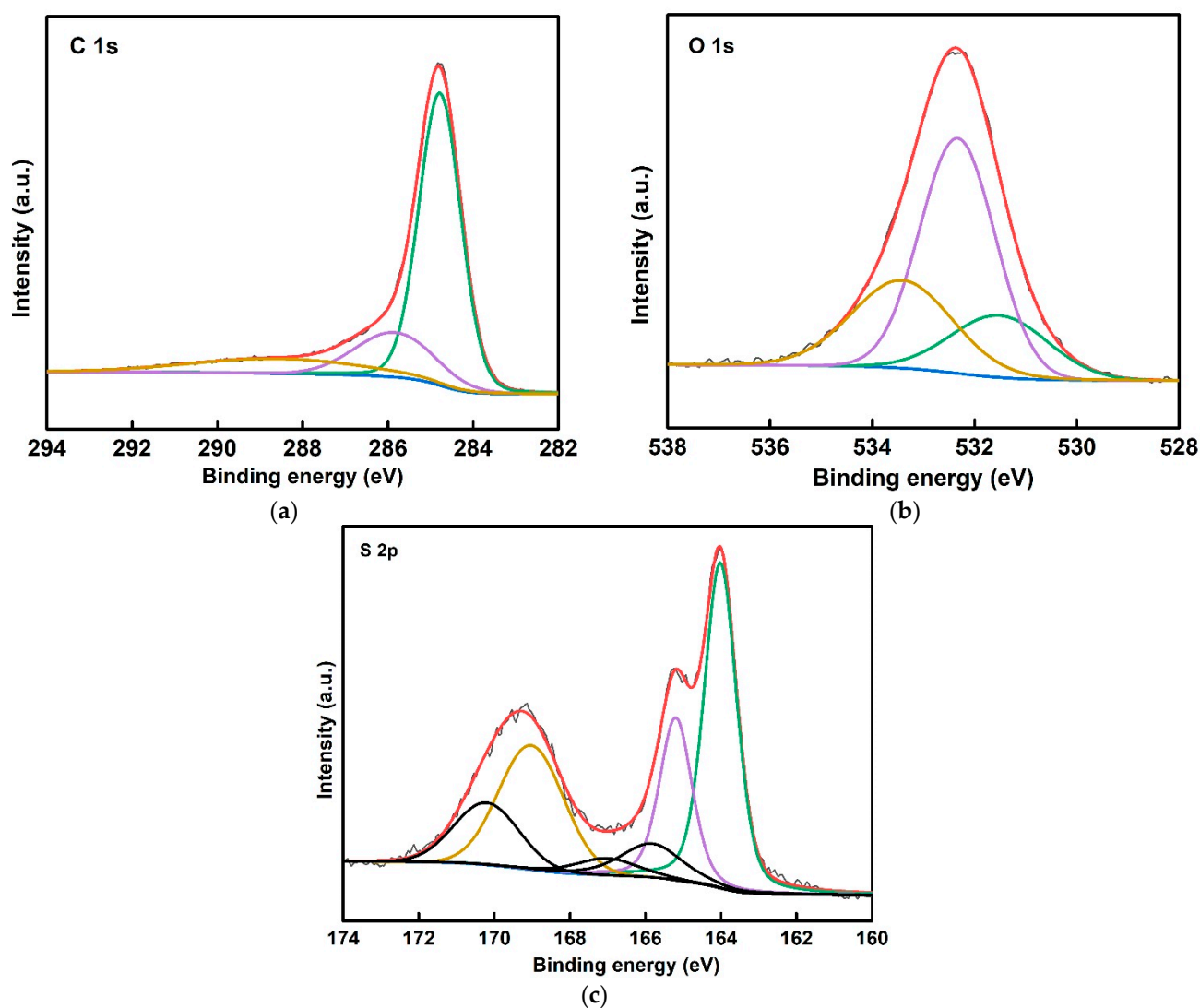


Figure 5. XPS spectra of S-C for (a) C 1s, (b) O 1s, and (c) S 2p.

4.2. Hg^0 Adsorption Capacity Tests

Figure 6 shows the Hg^0 adsorption performances of S-Cs with various HF etching times. As shown, the normalized-outlet Hg^0 concentration of S-C without etching climbed dramatically to above 0.90. Thus, the S-C without etching has a poor Hg^0 adsorption performance, and the removal rate of Hg^0 is only below 10%. However, after the HF etching, the S-C displayed far superior Hg^0 removal performances. The HF etching times played significant roles in the Hg^0 adsorption of S-C. After etching for 5 h, the concentration of Hg^0 at the normalized outlet remained below 0.2. With the extension of the etching time to 10 h, the Hg^0 adsorption performance of S-C can be further improved. However, a too-long etching time resulted in a decrease in Hg^0 adsorption performance. This is attributed to the fact that HF etching can remove the SiO_2 template to generate abundant pores on S-C, which allows for accessible mercury molecule transportation. As a result, the sulfur in S-C can be accessible sufficiently for binding mercury. However, the excessive etching will result in the collapse of the framework of carbons, hence the weakening of the Hg^0 adsorption on S-C.

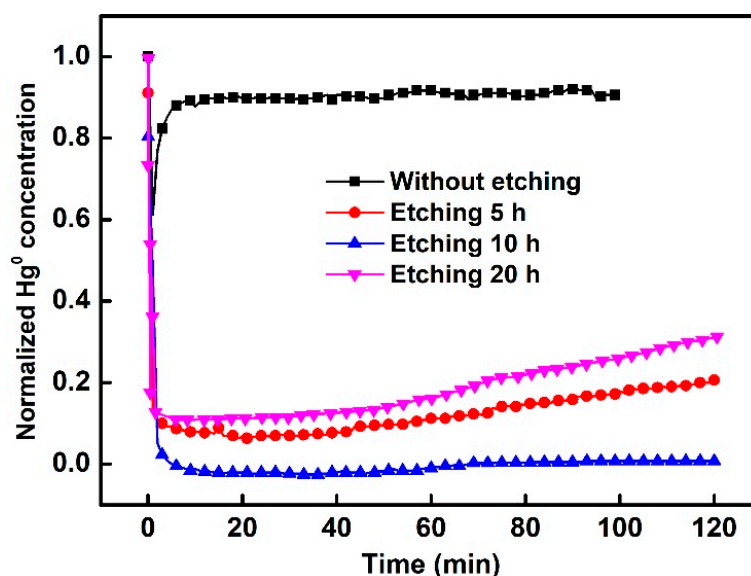


Figure 6. Hg^0 removal performances of S-C with different etching times.

The saturated adsorption capacity of an adsorbent is an important index to use to evaluate the adsorption performances of materials, so it is necessary to study the change in S-C adsorption capacity with time. The curve of Hg^0 adsorption capacity changing over time is shown in Figure 7. When the reaction duration was 1200 min, the adsorption capacity of Hg^0 exceeded 50% and reached $45.39 \text{ mg}\cdot\text{g}^{-1}$. In addition, it can be seen from the figure that the adsorption rate increases first and then decreases with time, and the slope is zero when the adsorption is saturated. Adsorption kinetic models can be adopted to investigate the process of Hg^0 adsorption and the dominant controlling factors. The pseudo-first-order-based kinetic model is the most common adsorption kinetic model. $\ln(q_e - q_t)$ is used to plot t , and the adsorption mechanism conforms to the pseudo-first-order model if a straight line can be obtained. The pseudo-second-order model is based on the assumption that the adsorption rate is controlled by the chemisorption mechanism. Elovich describes a series of reaction mechanism processes, which are suitable for processes with large activation energy changes in reactions and for complex heterogeneous diffusion processes. The intra-particle diffusion model is commonly used to analyze the control steps in the reaction. Generally, the material adsorption process is divided into two processes: adsorbent surface adsorption and slow pore diffusion. If the fitting result fails to reach the origin, it indicates that the internal diffusion of the material is not the only step to controlling the adsorption process. As shown in Figure 8, the pseudo-first-order model was closest to the adsorption process of Hg^0 on S-C, with an extremely high correlation coefficient ($R^2 = 0.9982$). The saturation adsorption capacity of S-C was simulated as $89.90 \text{ mg}\cdot\text{g}^{-1}$. When the molar ratio of $\text{Hg}:\text{S}$ is 1:1, it is equivalent to 55% of the sulfur accessibility in Hg^0 adsorption. For comparison, the Hg^0 saturation adsorption capacity of a sulfur-loaded commercial activated carbon (S/C) was also investigated. It should be noted that the S/C possessed a higher sulfur content and surface area compared with S-C. However, the saturation adsorption capacity of S/C was less than $1 \text{ mg}\cdot\text{g}^{-1}$, which was much lower compared with its theoretical adsorption capacity of $352.1 \text{ mg}\cdot\text{g}^{-1}$. Thus, most of the sulfur in S/C was not adopted sufficiently for binding mercury, although it possessed a higher surface area. It fully shows that the key to Hg^0 adsorption improvements lies in the high dispersion of active sulfur species [53]. Thus, the molten-salt pyrolysis synthesis strategy toward sulfur-functionalized carbon would be more superior compared with other traditional methods, such as impregnation when significantly dispersing the active components (i.e., sulfur).

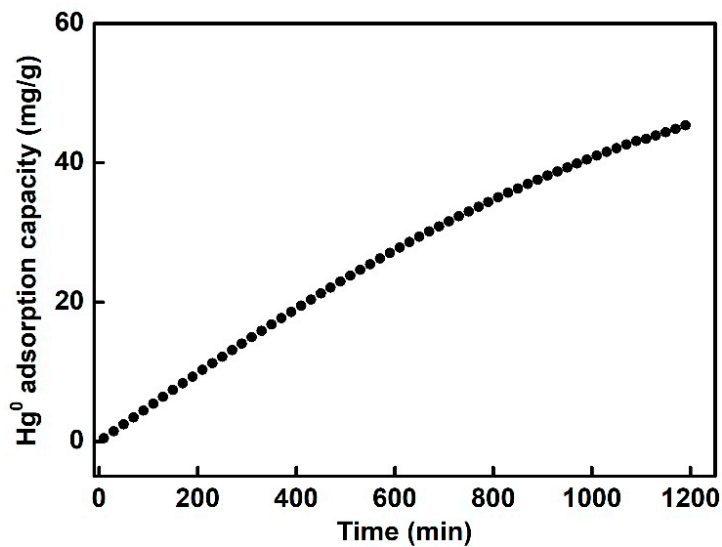


Figure 7. Hg^0 adsorption-capacity curve for S-AC as a function of time.

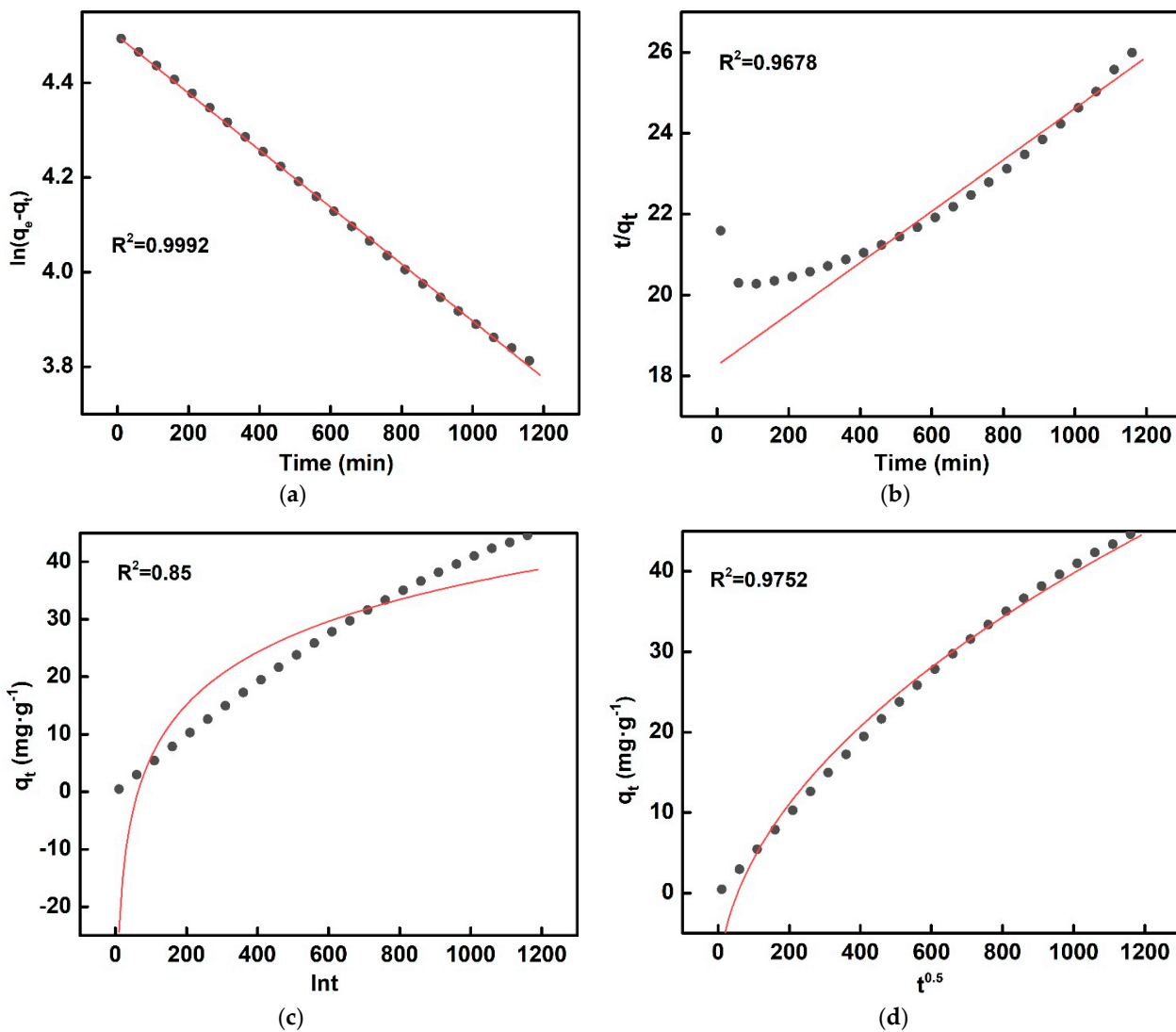


Figure 8. Hg^0 adsorption behaviors of S-C simulated by the (a) pseudo-first-order, (b) pseudo-second-order, (c) Elovich, and (d) intra-particle diffusion models.

4.3. Impact of Operation Conditions on Hg^0 Adsorption Capacity

An excellent adsorbent should have a good stability at various conditions. Figure 9 shows the influence of temperature on the Hg^0 adsorption capacities of S-C and S/C. The normalized-outlet Hg^0 concentration when passing through the S-C was maintained below 0.05 in a wide reaction temperature range of 25–125 °C. This suggests that an above 95% Hg^0 adsorption efficiency was obtained; even the sorbent dosage was as low as 5 mg. This wide temperature range proves that the S-C can be applied flexibly at different scenes for Hg^0 removal. In contrast, the S/C exhibited significantly different Hg^0 adsorption capacities under various temperatures, in which relatively limited Hg^0 adsorption capacities were obtained at low temperatures. Even at the optimum reaction temperature and the same amount of adsorbent, the concentration of Hg^0 at the normalized outlet is still higher than 0.15, much higher than S-C. Depending on the preferred temperature range, setting the S/C upstream of the ESP is the ideal application in which the Hg^0 adsorption capacity of S-C might be affected by various flue gas components, such as high concentrations of fly ash, SO_2 , and NO_2 .

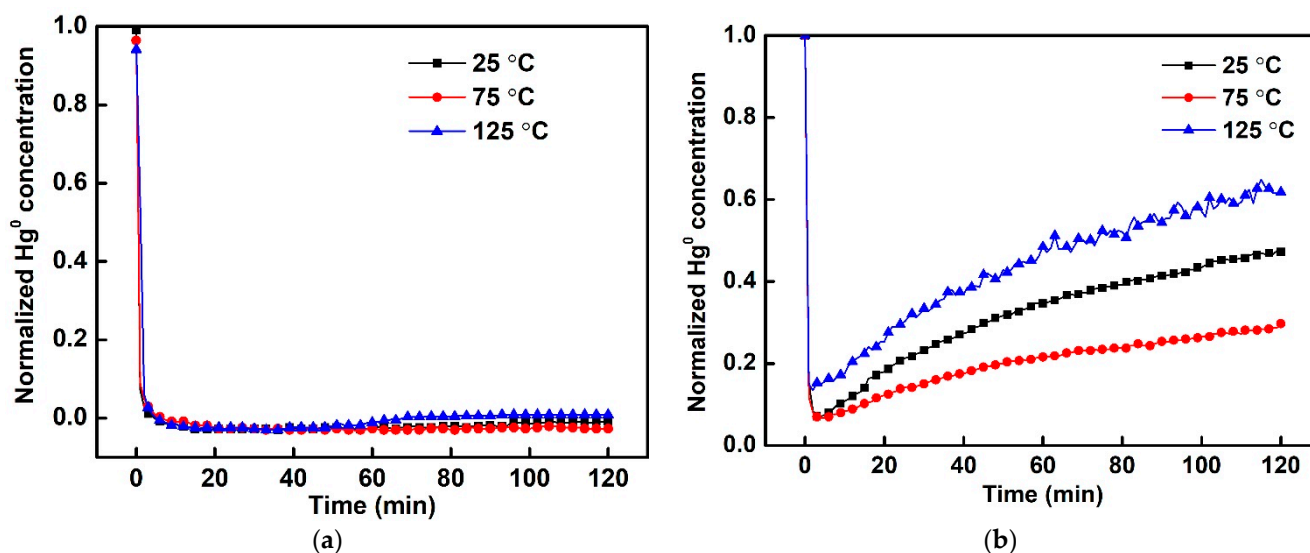


Figure 9. Hg^0 removal performances of (a) S-C and (b) S/C under different temperatures.

According to previous studies, SO_2 and H_2O generally compete with Hg^0 for adsorption sites, hence exhibiting inhibitive effects on the Hg^0 removal over carbonaceous sorbents [54,55]. However, the S-C exhibited an excellent resistance to these detrimental flue gas components. Figure 10a–c show that, in the presence of SO_2 , H_2O , as well as NO , the Hg^0 removal performance was very similar to that under a pure N_2 atmosphere. Even adding 1200 ppm of SO_2 , 12% H_2O , or 400 ppm of NO , the normalized-outlet Hg^0 concentration was kept at less than 0.05. As a direct comparison, the adsorption performance of S/C for Hg^0 was investigated. As shown in Figure 10d, the SO_2 , H_2O , and NO significantly weakened the adsorption capacity of S/C. These results could fully demonstrate the excellent resistance of S-C to the detrimental impacts of flue gas impurities compared with commercial activated carbon, which would facilitate the real-world applications.

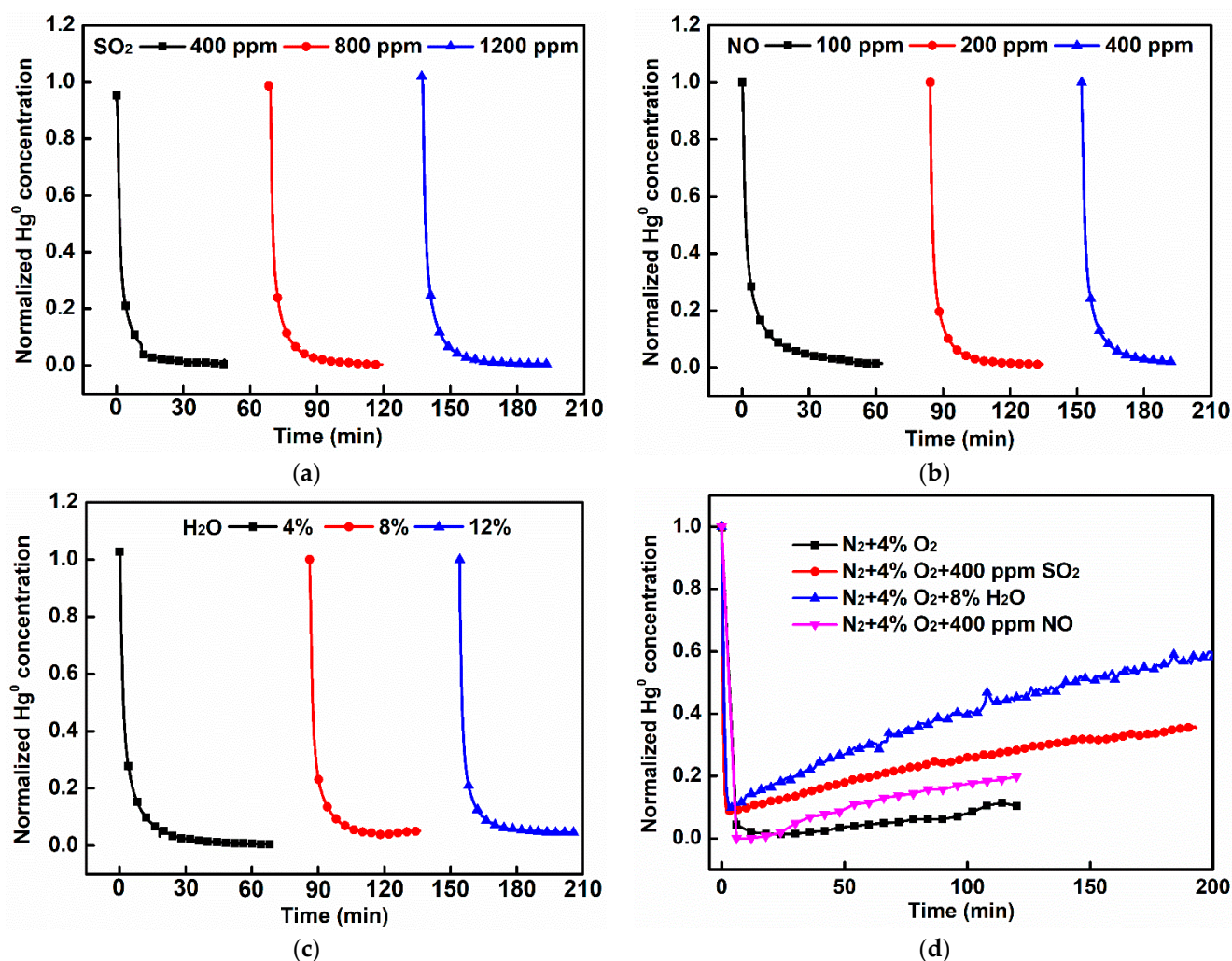


Figure 10. Effects of (a) SO₂, (b) NO, and (c) H₂O on the Hg⁰ removal performances of S-Cs and (d) effects of flue gas components on the Hg⁰ removal performances of S/Cs.

4.4. Reaction Mechanism

To study the mechanism of a Hg⁰ removal on S-C, the valence states of elements on spent S-C after adsorbing mercury were investigated by using XPS. Figure 11a shows that there is no significant change in the spectral binding energy of C 1s for the spent adsorbent, indicating that C did not participate in the Hg⁰ adsorption [56]. Figure 11b shows the O 1s spectra for the spent adsorbent. The spectra of O 1s can be divided into four separate corresponding peaks: C = O, C-O-C, COOH, and H₂O at 531.3, 532.5, 533.8, and 536.1 eV, respectively [57]. After the Hg⁰ adsorption, part of the C-O groups changed to C = O, and H₂O was generated on the adsorbent surface, which may have been caused by a charge imbalance after binding Hg⁰. Figure 11c shows the S 2p for the spent adsorbent, including only two peaks: C-S at 163.94 eV and thiophene at 165.22 eV [58]. The transformations of sulfur species on the spent adsorbent indicate that sulfur played a crucial role in the Hg⁰ removal. The absolute content of thiophene and C-S decreased after adsorbing Hg⁰, especially the peaks for sulfoxide, which disappeared compared with the fresh adsorbent. This variation indicates that thiophene (i.e., -C-S_x-C-, x = 1-2), sulfoxide, and C-S were beneficial to improving the Hg⁰ removal capacity. This is in line with a previous study [59], i.e., findings that the sulfur in sulfide existing in a low state as well as the reducing sulfur (such as thiosulfone) had a high affinity with the Hg⁰ atom. Electrons around the sulfur atom were easy to combine with Hg⁰, which was conducive to the removal of mercury. Figure 11d shows that the two peaks of Hg 4f corresponded to the peaks of 103 and 107

eV of HgS [60], further demonstrating that the sulfur in the adsorbent was active for binding Hg⁰.

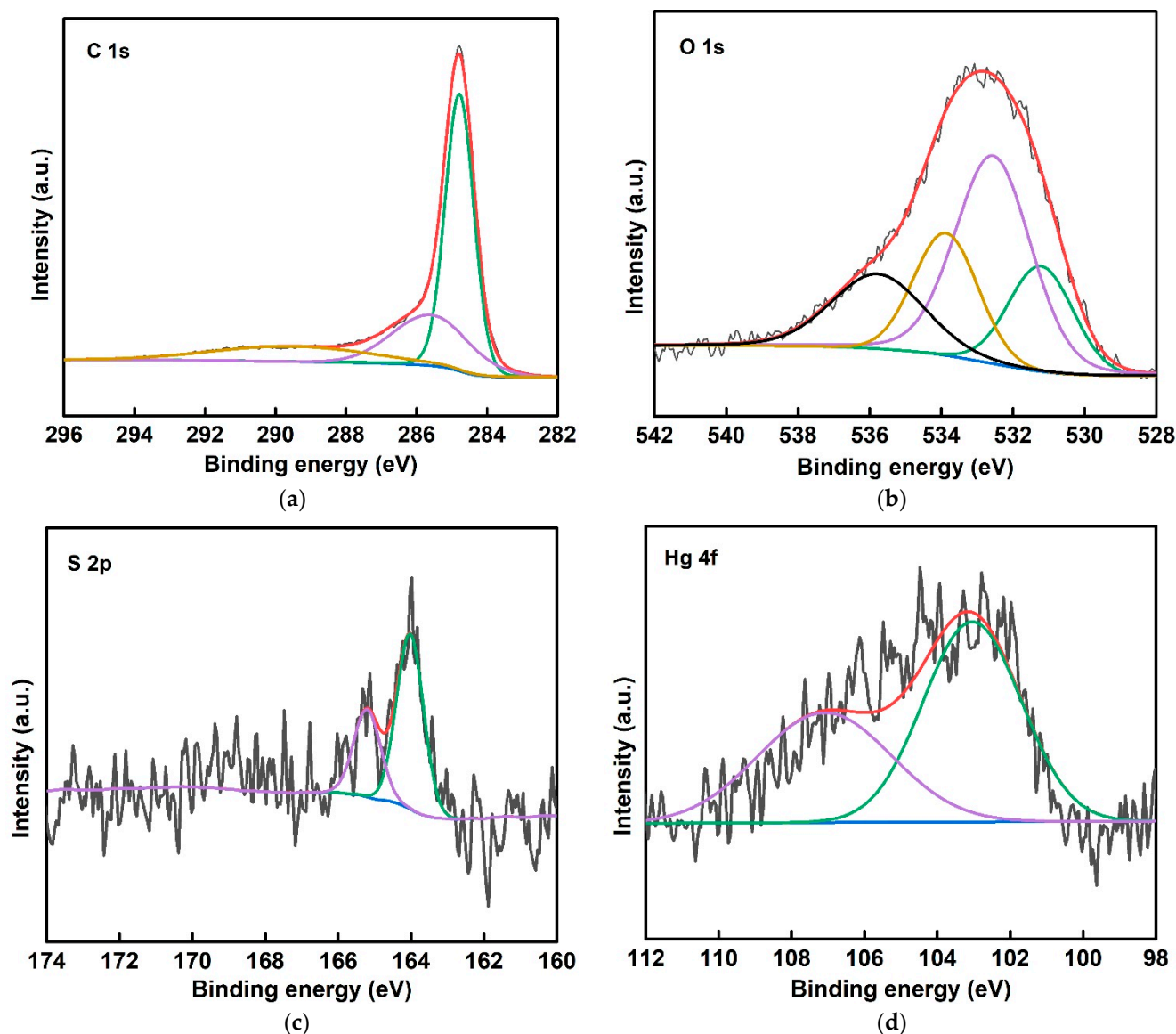


Figure 11. (a) C 1s, (b) O 1s, (c) S 2p, and (d) Hg 4f spectra of spent S-C.

5. Conclusions

Sulfur-functionalized carbon (S-C) derived from a molten-salt pyrolysis strategy was employed for a Hg⁰ removal. Abundant pores could be generated by using a SiO₂ hard template and a subsequent HF etching step. The HF etching time significantly affected the Hg⁰ removal performances of S-Cs. With an HF etching time of 10 h, the S-C presented the best Hg⁰ removal performance, the saturation Hg⁰-adsorption capacity of which reached 89.90 mg·g⁻¹. This value far exceeded that of the commercial sulfur-loaded activated carbon (S/C), which was specialized for Hg⁰ removals. The S-C displayed a good applicability at 25–125 °C, while the S/C could be adopted around only 125 °C since the Hg⁰ adsorption performances decreased when deviating from this temperature. The SO₂, NO, and H₂O had negligible adverse effects on Hg⁰ adsorption over S-C. The good Hg⁰ removal performance of S-C was ascribed to the existence of reduced sulfurs, such as thiophene, sulfoxide, and C-S, which have high affinities toward Hg⁰, and the fact that gaseous Hg⁰ was converted into HgS after the adsorption. These results indicate that molten-salt pyrolysis

can simultaneously achieve the carbonization and functionalization of sulfur-containing organic precursors and is an ideal method for preparing carbonaceous adsorbents for Hg⁰ removal.

Author Contributions: Conceptualization, J.Y.; Writing—original draft, J.Y.; Formal analysis, J.Y.; Investigation, H.X.; Writing—review & editing, H.X.; Software, F.M. and W.Q.; Methodology, F.M.; Supervision, Q.G.; Validation, Q.G., T.H. and Z.Y.; Data curation, T.H. and W.Q.; Visualization, Z.Y.; Resources, H.L.; Project administration, H.L. All authors have read and agreed to the published version of the manuscript.

Funding: This research received no external funding.

Institutional Review Board Statement: Not applicable.

Informed Consent Statement: Not applicable.

Data Availability Statement: No data was reported.

Acknowledgments: This project was supported by the National Natural Science Foundation of China (51906260), the Natural Science Foundation of Hunan Province, China (2021JJ30851), the Postgraduate Scientific Research Innovation Project of Hunan Province (CX20210098), the Foundation of State Key Laboratory of High-efficiency Utilization of Coal and Green Chemical Engineering (Grant No. 2022-K09 and 2022-K52), and the Key Research and Development Program of Sichuan Province (2021YFG0117).

Conflicts of Interest: The authors declare no conflict of interest.

References

1. Landrigan, P.J.; Wright, R.O.; Birnbaum, L.S. Mercury toxicity in children. *Science* **2013**, *342*, 1447. [[CrossRef](#)] [[PubMed](#)]
2. Richardson, J.B.; Moore, L. A tale of three cities: Mercury in urban deciduous foliage and soils across land-uses in Poughkeepsie NY, Hartford CT, and Springfield MA USA. *Sci. Total Environ.* **2020**, *715*, 136869. [[CrossRef](#)] [[PubMed](#)]
3. Li, M.; Yang, H.E.; Lu, H.; Wu, T.; Zhou, D.; Liu, Y. Investigation into the Classification of Tight Sandstone Reservoirs via Imbibition Characteristics. *Energies* **2018**, *11*, 2619. [[CrossRef](#)]
4. Masoomi, I.; Kamata, H.; Yukimura, A.; Ohtsubo, K.; Schmid, M.O.; Scheffknecht, G. Investigation on the behavior of mercury across the flue gas treatment of coal combustion power plants using a lab-scale firing system. *Fuel Process. Technol.* **2020**, *201*, 106340. [[CrossRef](#)]
5. Lee, S.S.; Wilcox, J. Behavior of mercury emitted from the combustion of coal and dried sewage sludge: The effect of unburned carbon, Cl, Cu and Fe. *Fuel* **2017**, *203*, 749–756. [[CrossRef](#)]
6. Yang, S.; Liu, C.; Wang, P.; Yi, H.; Shen, F.; Liu, H. Co₉S₈ nanoparticles-embedded porous carbon: A highly efficient sorbent for mercury capture from nonferrous smelting flue gas. *J. Hazard. Mater.* **2021**, *412*, 124970. [[CrossRef](#)]
7. Fernández-Miranda, N.; Rodríguez, E.; Lopez-Anton, M.; García, R.; Martínez-Tarazona, M. A New Approach for Retaining Mercury in Energy Generation Processes: Regenerable Carbonaceous Sorbents. *Energies* **2017**, *10*, 1311. [[CrossRef](#)]
8. Mei, J.; Liao, Y.; Qin, R.; Sun, P.; Wang, C.; Ma, Y.; Qu, Z.; Yan, N.; Yang, S. Acceleration of Hg⁰ adsorption onto natural sphalerite by Cu²⁺ activation during flotation: Mechanism and applications in Hg⁰ recovery. *Environ. Sci. Technol.* **2020**, *54*, 7687–7696. [[CrossRef](#)]
9. Yu, M.Y.; Luo, G.Q.; Sun, R.Z.; Zou, R.J.; Li, X.; Yao, H. A mechanism study on effects of bromide ion on mercury re-emission in WFGD slurry. *Chem. Eng. J.* **2021**, *406*, 127010. [[CrossRef](#)]
10. Zhang, Y.; Yang, J.; Yu, X.; Sun, P.; Zhao, Y.; Zhang, J.; Chen, G.; Yao, H.; Zheng, C. Migration and emission characteristics of Hg in coal-fired power plant of China with ultra low emission air pollution control devices. *Fuel Process. Technol.* **2017**, *158*, 272–280. [[CrossRef](#)]
11. Wen, M.; Wu, Q.; Li, G.; Wang, S.; Li, Z.; Tang, Y.; Xu, L.; Liu, T. Impact of ultra-low emission technology retrofit on the mercury emissions and cross-media transfer in coal-fired power plants. *J. Hazard. Mater.* **2020**, *396*, 122729. [[CrossRef](#)] [[PubMed](#)]
12. Zhang, X.; Cui, L.; Li, Y.; Zhao, Y.; Dong, Y.; Cao, S. Adsorption and oxidation of mercury by montmorillonite powder modified with different copper compounds. *Energy Fuels* **2019**, *33*, 7852–7860. [[CrossRef](#)]
13. Heidel, B.; Klein, B. Reemission of elemental mercury and mercury halides in wet flue gas desulfurization. *Int. J. Coal. Geol.* **2017**, *170*, 28–34. [[CrossRef](#)]
14. Jia, T.; Ji, Z.; Wu, J.; Zhao, X.; Wang, F.; Xiao, Y.; Qi, X.; He, P.; Li, F. Nanosized ZnIn₂S₄ supported on facet-engineered CeO₂ nanorods for efficient gaseous elemental mercury immobilization. *J. Hazard. Mater.* **2021**, *419*, 126436. [[CrossRef](#)] [[PubMed](#)]
15. Xu, H.; Qu, Z.; Zong, C.; Quan, F.; Mei, J.; Yan, N. Catalytic oxidation and adsorption of Hg⁰ over low-temperature NH₃-SCR LaMnO₃ perovskite oxide from flue gas. *Appl. Catal. B* **2016**, *186*, 30–40. [[CrossRef](#)]

16. Choi, S.; Lee, S.S. Mercury adsorption characteristics of Cl-impregnated activated carbons in simulated flue gases. *Fuel* **2021**, *299*, 120822. [[CrossRef](#)]
17. Dastgheib, S.A.; Mock, J.; Ilangovan, T. Evaluation of modified activated carbons for mercury reemission control during neutralization of a simulated wastewater from the direct contact cooler of a pressurized oxy-combustion process. *Ind. Eng. Chem. Res.* **2021**, *60*, 947–954. [[CrossRef](#)]
18. Huang, T.F.; Duan, Y.F.; Luo, Z.K.; Zhao, S.L.; Geng, X.Z.; Xu, Y.F.; Huang, Y.J.; Wei, H.Q.; Ren, S.J.; Wang, H.; et al. Influence of flue gas conditions on mercury removal by activated carbon injection in a pilot-scale circulating fluidized bed combustion system. *Ind. Eng. Chem. Res.* **2019**, *58*, 15553–15561. [[CrossRef](#)]
19. Zhao, W.M.; Geng, X.Z.; Lu, J.C.; Duan, Y.F.; Liu, S.; Hu, P.; Xu, Y.F.; Huang, Y.J.; Tao, J.; Gu, X.B. Mercury removal performance of brominated biomass activated carbon injection in simulated and coal-fired flue gas. *Fuel* **2021**, *285*, 119131. [[CrossRef](#)]
20. Liu, D.J.; Li, B.; Liu, Y.X.; Wu, J. Copper sulfide-loaded boron nitride nanosheets for elemental mercury removal from simulated flue gas. *Energy Fuel* **2021**, *35*, 2234–2242. [[CrossRef](#)]
21. Park, J.; Lee, S.S. Adsorption of mercury by activated carbon prepared from dried sewage sludge in simulated flue gas. *J. Air Waste Manag. Assoc.* **2018**, *68*, 1077–1084. [[CrossRef](#)] [[PubMed](#)]
22. Yang, Z.; Li, H.; Liao, C.; Zhao, J.; Feng, S.; Li, P.; Liu, X.; Yang, J.; Shih, K. Magnetic rattle-type Fe₃O₄@CuS nanoparticles as recyclable sorbents for mercury capture from coal combustion flue gas. *ACS Appl. Nano Mater.* **2018**, *1*, 4726–4736. [[CrossRef](#)]
23. Oliveira, L.C.A.; Rios, R.V.R.A.; Fabris, J.D.; Garg, V.; Sapag, K.; Lago, R.M. Activated carbon/iron oxide magnetic composites for the adsorption of contaminants in water. *Carbon* **2002**, *40*, 2177–2183. [[CrossRef](#)]
24. Padak, B.; Wilcox, J. Understanding mercury binding on activated carbon. *Carbon* **2009**, *47*, 2855–2864. [[CrossRef](#)]
25. Li, H.; Zhu, L.; Wang, J.; Li, L.; Shih, K. Development of nano-sulfide sorbent for efficient removal of elemental mercury from coal combustion fuel gas. *Environ. Sci. Technol.* **2016**, *50*, 9551–9557. [[CrossRef](#)] [[PubMed](#)]
26. Qiao, G.; Liu, L.; Hao, X.; Zheng, J.; Liu, W.; Gao, J.; Zhang, C.C.; Wang, Q. Signal transduction from small particles: Sulfur nanodots featuring mercury sensing, cell entry mechanism and in vitro tracking performance. *Chem. Eng. J.* **2020**, *382*, 122907. [[CrossRef](#)]
27. Zhao, L.; Wu, Y.-W.; Han, J.; Wang, H.-X.; Liu, D.-J.; Lu, Q.; Yang, Y.-P. Density Functional Theory Study on Mechanism of Mercury Removal by CeO₂ Modified Activated Carbon. *Energies* **2018**, *11*, 2872. [[CrossRef](#)]
28. Manceau, A.; Merkulova, M.; Murdzek, M.; Batanova, V.; Baran, R.; Glatzel, P.; Saikia, B.K.; Paktunc, D.; Leticariu, L. Chemical Forms of Mercury in Pyrite: Implications for Predicting Mercury Releases in Acid Mine Drainage Settings. *Environ. Sci. Technol.* **2018**, *52*, 10286–10296. [[CrossRef](#)]
29. Deng, J.; Li, M.; Wang, Y. Biomass-derived carbon: Synthesis and applications in energy storage and conversion. *Green Chem.* **2016**, *18*, 4824–4854. [[CrossRef](#)]
30. Wang, W.; Lu, Y.C.; Huang, H.; Wang, A.J.; Chen, J.R.; Feng, J.J. Solvent-free synthesis of sulfur- and nitrogen-co-doped fluorescent carbon nanoparticles from glutathione for highly selective and sensitive detection of mercury(II) ions. *Sens. Actuators B Chem.* **2014**, *202*, 741–747. [[CrossRef](#)]
31. Ma, J.; Zhou, B.; Zhang, H.; Zhang, W. Fe/S modified sludge-based biochar for tetracycline removal from water. *Powd. Technol.* **2020**, *364*, 889–900. [[CrossRef](#)]
32. Shin, Y.; Fryxell, G.E.; Um, W.; Parker, K.; Mattigod, S.V.; Skaggs, R. Sulfur-Functionalized Mesoporous Carbon. *Adv. Funct. Mater.* **2007**, *17*, 2897–2901. [[CrossRef](#)]
33. Marczak-Grzesik, M.; Budzyn, S.; Tora, B.; Szufa, S.; Kogut, K.; Burmistrz, P. Low-cost organic adsorbents for elemental mercury removal from lignite flue gas. *Energies* **2021**, *14*, 2174. [[CrossRef](#)]
34. Gwenzi, W.; Chaukura, N.; Wenga, T.; Mtisi, M. Biochars as media for air pollution control systems: Contaminant removal, applications and future research directions. *Sci. Total Environ.* **2021**, *753*, 142249. [[CrossRef](#)]
35. Shen, B.; Li, G.; Wang, F.; Wang, Y.; He, C.; Zhang, M.; Singh, S. Elemental mercury removal by the modified bio-char from medicinal residues. *Chem. Eng. J.* **2015**, *272*, 28–37. [[CrossRef](#)]
36. Li, G.; Wang, S.; Wang, F.; Wu, Q.; Tang, Y.; Shen, B. Role of inherent active constituents on mercury adsorption capacity of chars from four solid wastes. *Chem. Eng. J.* **2017**, *307*, 544–552. [[CrossRef](#)]
37. Wang, L.; Chen, M.X.; Yan, Q.Q.; Xu, S.L.; Chu, S.Q.; Chen, P.; Lin, Y.; Liang, H.W. A sulfur-tethering synthesis strategy toward high-loading atomically dispersed noble metal catalysts. *Sci. Adv.* **2019**, *5*, 6322. [[CrossRef](#)]
38. Wu, Z.Y.; Xu, S.L.; Yan, Q.Q.; Chen, Z.Q.; Ding, Y.W.; Li, C.; Liang, H.W.; Yu, S.H. Transition metal-assisted carbonization of small organic molecules toward functional carbon materials. *Sci. Adv.* **2018**, *4*, 0788. [[CrossRef](#)]
39. Xu, Y.; Luo, G.; Zhang, Q.; Li, Z.; Zhang, S.; Cui, W. Cost-effective sulfurized sorbents derived from one-step pyrolysis of wood and scrap tire for elemental mercury removal from flue gas. *Fuel* **2021**, *285*, 119221. [[CrossRef](#)]
40. Shen, B.; Liu, Z.; Xu, H.; Wang, F. Enhancing the absorption of elemental mercury using hydrogen peroxide modified bamboo carbons. *Fuel* **2019**, *235*, 878–885. [[CrossRef](#)]
41. Yang, J.; Xu, H.; Zhao, Y.; Li, H.; Zhang, J. Mercury Removal from Flue Gas by Noncarbon Sorbents. *Energy Fuel* **2021**, *35*, 3581–3610. [[CrossRef](#)]
42. Yang, J.; Li, Q.; Zu, H.; Yang, Z.; Qu, W.; Li, M.; Li, H. Surface-engineered sponge decorated with copper selenide for highly efficient gas-phase mercury immobilization. *Environ. Sci. Technol.* **2020**, *54*, 16195–16203. [[CrossRef](#)] [[PubMed](#)]

43. Yang, Z.; Yang, J.; Li, H.; Qu, W.; Leng, L.; Zhao, J.; Feng, Y.; Xu, Z.; Liu, H.; Shih, K. Advances in magnetically recyclable remediators for elemental mercury degradation in coal combustion flue gas. *J. Mater. Chem. A* **2020**, *8*, 18624–18650. [[CrossRef](#)]
44. Yang, J.; Zhao, Y.; Ma, S.; Zhu, B.; Zhang, J.; Zheng, C. Mercury removal by magnetic biochar derived from simultaneous activation and magnetization of sawdust. *Environ. Sci. Technol.* **2016**, *50*, 12040–12047. [[CrossRef](#)]
45. Revellame, E.D.; Fortela, D.L.; Sharp, W.; Hernandez, R.; Zappi, M.E. Adsorption kinetic modeling using pseudo-first order and pseudo-second order rate laws: A review. *Cleaner Eng. Technol.* **2020**, *1*, 100032. [[CrossRef](#)]
46. Pichler, C.; Lackner, R. Post-peak decelerating reaction of Portland cement: Monitoring by heat flow calorimetry, modelling by Elovich-Landsberg model and reaction-order model. *Constr. Build. Mater.* **2020**, *231*, 117107. [[CrossRef](#)]
47. Cabooter, D.; Song, H.; Makey, D.; Sadriaj, D.; Dittmann, M.; Stoll, D.; Desmet, G. Measurement and modelling of the intra-particle diffusion and b-term in reversed-phase liquid chromatography. *J. Chromatogr. A* **2021**, *1637*, 461852. [[CrossRef](#)]
48. Yang, J.; Li, Q.; Zhu, W.; Qu, W.; Li, M.; Xu, Z.; Yang, Z.; Liu, H.; Li, H. Recyclable chalcopyrite sorbent for mercury removal from coal combustion flue gas. *Fuel* **2021**, *290*, 120049. [[CrossRef](#)]
49. Cheng, F.; Zhou, P.; Huo, X.; Liu, Y.; Liu, Y.; Zhang, Y. Enhancement of bisphenol A degradation by accelerating the Fe(III)/Fe(II) cycle in graphene oxide modified Fe(III)/peroxymonosulfate system under visible light irradiation. *J. Colloid Interf. Sci.* **2020**, *580*, 1021. [[CrossRef](#)]
50. Feng, P.; Wang, W.; Wang, K.; Cheng, S.; Jiang, K. A high-performance carbon with sulfur doped between interlayers and its sodium storage mechanism as anode material for sodium ion batteries. *J. Alloys Compd.* **2019**, *795*, 223–232. [[CrossRef](#)]
51. Yu, H.; Qian, C.; Ren, H.; Chen, M.; Tang, D.; Wu, H.; Lv, R. Enhanced catalytic properties of bimetallic sulfides with the assistance of graphene oxide for accelerating triiodide reduction in dye-sensitized solar cells. *Sol. Energy* **2020**, *207*, 1037–1044. [[CrossRef](#)]
52. Wen, X.; Zhao, Z.; Zhai, S.; Wang, X.; Li, Y. Stable nitrogen and sulfur co-doped carbon dots for selective folate sensing, in vivo imaging and drug delivery. *Diam. Relat. Mater.* **2020**, *105*, 107791. [[CrossRef](#)]
53. Asasian, N.; Kaghazchi, T.; Faramarzi, A.; Hakimi-Siboni, A.; Asadi-Kesheh, R.; Kavand, M.; Mohtashami, S.-A. Enhanced mercury adsorption capacity by sulfurization of activated carbon with SO₂ in a bubbling fluidized bed reactor. *J. Taiwan Inst. Chem. E.* **2014**, *45*, 1588–1596. [[CrossRef](#)]
54. Guo, Y.; Niu, J.; Zhang, H.; Cheng, F.; Wu, H.; Jin, D. Enhanced SO₂ and Rhodamine B Removal by Blending Coke-Making Waste Benzene Residue (BR) for Pelletized Activated Coke (PAC) Production and Mechanisms. *Energy Fuel* **2019**, *33*, 5173–5181. [[CrossRef](#)]
55. Liu, H.; Xie, X.; Chen, H.; Yang, S.; Liu, C.; Liu, Z.; Yang, Z.; Li, Q.; Yan, X. SO₂ promoted ultrafine nano-sulfur dispersion for efficient and stable removal of gaseous elemental mercury. *Fuel* **2020**, *261*, 116367. [[CrossRef](#)]
56. Zhou, M.; Xie, X.; Liu, Q.; Zhang, M.; Peng, C.; Li, F.; Liu, Q.; Song, Y.; Wu, J.; Qiao, Z. Spherical In₂S₃ anchored on g-C₃N₄ nanosheets for efficient elemental mercury removal in the wide temperature range. *Chem. Eng. J.* **2022**, *430*, 132857. [[CrossRef](#)]
57. Alegre, C.; Sebastián, D.; Lázaro, M.J. Carbon xerogels electrochemical oxidation and correlation with their physico-chemical properties. *Carbon* **2019**, *144*, 382–394. [[CrossRef](#)]
58. Hsu, C.J.; Chiou, H.J.; Chen, Y.H.; Lin, K.S.; Rood, M.J.; Hsi, H.C. Mercury adsorption and re-emission inhibition from actual WFGD wastewater using sulfur-containing activated carbon. *Environ. Res.* **2019**, *168*, 319–328. [[CrossRef](#)]
59. Zhao, S.; Luo, H.; Ma, A.; Sun, Z.; Zheng, R. Experimental study on mercury removal from coal-fired flue gas by sulfur modified biomass coke with mechanochemical method. *Fuel* **2022**, *309*, 122201. [[CrossRef](#)]
60. Yang, Q.; Yang, Z.; Li, H.; Zhao, J.; Yang, J.; Qu, W.; Shih, K. Selenide functionalized natural mineral sulfides as efficient sorbents for elemental mercury capture from coal combustion flue gas. *Chem. Eng. J.* **2020**, *398*, 125611. [[CrossRef](#)]